RSC Advances

PAPER

View Article Online
View Journal | View Issue

Cite this: *RSC Adv.*, 2026, **16**, 25447

Gingerol-loaded hollow manganese dioxide nanoparticles attenuate intervertebral disc oxidative stress

Xu Liu,[a] Bolin Lu,[a] Yunqi Zhou,[a] Chengdong Zhang,[a] Feng Shi,[b] Gang Feng,[a] Xuwei Luo*[a] and Dongqin Xiao*[a]

Intervertebral disc degeneration (IVDD) is a major cause of chronic low back pain, thus therapies capable of halting its progression are urgently needed. Evidence suggests that oxidative stress is a key accelerator of IVDD, making interventions targeting reactive oxygen species (ROS) highly promising. The natural compound 6-gingerol has been proved to possess potent antioxidant properties, however, its therapeutic application is hampered by poor solubility, rapid clearance, and lack of targeted delivery. To address these limitations and investigate the effect of 6-gingerol on IVDD, we developed an integrated nanoplatform (H@G) by encapsulating 6-gingerol within hollow manganese dioxide nanoparticles. The synthesized H@G nanoparticles exhibited a uniform hollow spherical structure (~100 nm), a high surface area, and successful drug loading without altering the carrier morphology. The nanoparticles demonstrated good stability in physiological media but underwent rapid degradation under acidic conditions and in an H_2O_2 microenvironment. Accordingly, H@G exhibited pH- and H_2O_2-responsive drug release. The H@G nanoparticles also displayed superoxide dismutase-like, hydroxyl radical-scavenging, and catalase-like activities in a concentration-dependent manner. Under H_2O_2-induced oxidative stress, H@G significantly enhanced the viability of nucleus pulposus cells, potently scavenged both intracellular and mitochondrial ROS, restored mitochondrial membrane potential, and preserved cristae ultrastructure. Furthermore, H@G restored extracellular matrix homeostasis under oxidative stress by upregulating anabolic markers (ACAN and COL2A1) and downregulating catabolic enzymes (MMP3 and MMP13). Collectively, our results demonstrate that the H@G nanosystem effectively attenuates oxidative stress, maintains mitochondrial homeostasis, and promotes matrix anabolism in NPCs, which provides a promising and targeted strategy to attenuate oxidative stress and disc degeneration in IVDD.

Received 22nd January 2026
Accepted 21st April 2026

DOI: 10.1039/d6ra00597g

rsc.li/rsc-advances

1 Introduction

Intervertebral disc degeneration (IVDD) is a prevalent degenerative spinal disorder associated with global population aging, posing a substantial public health and socioeconomic burden.[1] Epidemiological data show that nearly 80% of adults experience low back pain at least once during their lifetime, of which approximately 10% progresses to functional impairment, significantly affecting work capacity and quality of life.[2,3] The prevalence of IVDD increases markedly with age, with the majority of individuals over 60 years old exhibiting varying degrees of disc degeneration. As global life expectancy continues to rise, the incidence of IVDD is expected to further increase.[4]

Current clinical management, divided into conservative treatments and surgical interventions, offers limited efficacy in altering disease progression. Conservative approaches, such as NSAIDs and physical therapy, primarily aim at symptom relief but are hindered by the disc's avascular nature and dense extracellular matrix, which restrict drug penetration and local bioavailability.[5,6] Surgical options, while effective for mechanical compression, are invasive and may accelerate adjacent segment degeneration.[7,8] This clear unmet clinical need underscores the imperative to develop targeted, disease-modifying therapies.

Accumulating evidence identifies oxidative stress as a central pathological driver in IVDD.[9] The disc's hypoxic and nutrient-deficient microenvironment predisposes nucleus pulposus cells (NPCs) to excessive reactive oxygen species (ROS) accumulation, which overwhelms endogenous antioxidant defenses.[10,11] This oxidative insult disrupts mitochondrial function and triggers a catabolic shift, leading to extracellular matrix (ECM) degradation and NPC death, thereby fueling a self-perpetuating cycle of degeneration.[12–14] Consequently,

[a]*Research Institute of Tissue Engineering and Stem Cells, Department of Orthopedics, the Second Clinical College of North Sichuan Medical College, Nanchong, Sichuan 637000, China. E-mail: ciciweiting@163.com; xiaodongqin@nsmc.edu.cn*
[b]*Collaboration Innovation Center for Tissue Repair Material Engineering Technology, China West Normal University, Nanchong, Sichuan 637002, China*

therapeutic strategies capable of interrupting this oxidative cascade are of significant interest.

In this context, nanotechnology-based drug delivery systems offer a transformative strategy to overcome the anatomical and biological barriers of the intervertebral disc.[15–17] Among various nanomaterials, hollow manganese dioxide (HM) nanoparticles are particularly promising due to their large hollow interior, mesoporous shell for high drug-loading capacity, intrinsic catalase-like activity for scavenging H_2O_2 and alleviating hypoxia, and favorable biodegradability.[18–20]

Parallel to advances in delivery platforms, the identification of bioactive compounds that can simultaneously target multiple degenerative pathways is a key research focus. Gingerol, especially its predominant form 6-gingerol (6-G), is a potent natural phenolic compound with documented anti-inflammatory, antioxidant, and anti-apoptotic properties.[21,22] Relevant studies have shown that 6-gingerol protects NPCs from H_2O_2 induced injury, suppresses pro-inflammatory cytokine production *via* NF-κB inhibition, and promotes anabolic gene expression (*e.g.*, COL2A1 and ACAN).[23,24] These multi-faceted actions establish gingerol as a promising candidate for therapeutic intervention in disc degeneration.

Therefore, we developed an integrated nanotherapeutic platform (H@G) by encapsulating 6-gingerol within HM nanocarriers. This dual-function system leverages the intrinsic catalytic activity of HM to remodel the pathological disc microenvironment while concurrently acting as a targeted delivery vehicle for gingerol. By enabling the *in situ* release of gingerol directly into degenerated disc tissue, the platform enhances the multifaceted cytoprotective effects of the compound on NPCs. Through synergistic modulation of both the extracellular niche and intracellular dysfunction, this strategy aims to promote holistic disc repair. By protecting NPCs, preserving mitochondrial function, and maintaining extracellular matrix homeostasis, it offers a novel nano-integrated therapeutic approach for intervertebral disc degeneration.

2 Materials and methods

2.1 Materials

Triethyl orthosilicate (TEOS), potassium permanganate ($KMnO_4$), sodium carbonate (Na_2CO_3), and a 30 wt% hydrogen peroxide (H_2O_2) solution were obtained from Aladdin (China). Dimethyl sulfoxide (DMSO), the CCK-8 assay kit, live/dead cell staining kit, ROS fluorescent probe kit, mitochondrial membrane potential assay kit, and Hoechst 33342 were sourced from Beyotime (China). MitoSOX Red was purchased from MedChemExpress (MCE, USA). The superoxide dismutase (SOD) assay kit and hydroxyl radical scavenging activity colorimetric assay kit were obtained from Elabscience (China). The catalase (CAT) activity assay kit was purchased from AIDACX (China). The ATP assay kit was obtained from Abbkine (China). DMEM/F12 medium, fetal bovine serum (FBS), penicillin/streptomycin, trypsin, and type II collagenase were acquired from Gibco (USA). Collagen type II alpha 1 chain (COL2A1), aggrecan (ACAN), matrix metallopeptidase 3 (MMP3), matrix metallopeptidase 13 (MMP13) were purchased from Proteintech (China). Goat Anti-Rabbit IgG H&L (HRP) were purchased from ZEN-BIOSCIENCE (China).

2.2 Synthesis of HM nanoparticles

HM nanoparticles were synthesized according to a template-based method.[25] Briefly, solid silica (SiO_2) nanoparticle templates were first prepared. A mixture containing 25 mL of anhydrous ethanol, 0.5 mL of deionized water, and 1.4 mL of $NH_3 \cdot H_2O$ was added to a 50 mL round-bottom flask and heated to 45 °C under magnetic stirring in an oil bath. After 10 minutes, 0.75 mL of tetraethyl orthosilicate was added dropwise, and the reaction was allowed to proceed at 45 °C for 3 hours. The resulting SiO_2 nanoparticles were collected by centrifugation and washed twice with ethanol and twice with deionized water before being resuspended in water for subsequent use.

To coat the silica templates with MnO_2, 150 mg of $KMnO_4$ dissolved in 50 mL of water was added dropwise to the SiO_2 nanoparticles suspension under ultrasonication. The mixture was stirred for 6 hours, with the water bath being replaced midway to maintain the temperature below 40 °C. The obtained SiO_2@MnO_2 core–shell nanoparticles were collected by centrifugation and washed three times with deionized water. Finally, the silica core was etched by dispersing the SiO_2@MnO_2 nanoparticles in 2 M Na_2CO_3 solution and incubating at 60 °C for 12 hours. The hollow HM nanoparticles were then collected by centrifugation and washed extensively with ultrapure water.

2.3 Preparation of H@G and determination of drug loading efficiency

6-Gingerol was dissolved in anhydrous DMSO to prepare a 20 mM stock solution. To prepare H@G at different concentrations, the HM concentration was fixed at 50 μg mL^{-1}, and different concentrations of 6-gingerol solution (diluted from the stock) were added. The H@G samples prepared with 6-gingerol input concentrations of 10 μM and 50 μM were designated as L–H@G and H–H@G, respectively. All H@G nanoparticles were collected by centrifugation and stored for subsequent use.

To measure the drug encapsulation efficiency and drug loading, the mixtures of HM and gingerol were centrifuged to separate the H@G from free gingerol. The supernatant containing free drug was collected and measured using the high-performance liquid chromatography (HPLC) at a detection wavelength of 280 nm. The H@G nanoparticles were freeze-dried and weighed. The encapsulation efficiency (EE) and drug loading content (DL) were calculated according to the following formulas:[26,27]

$$\mathrm{EE}(\%) = \frac{\text{total amount of drug-amount of free drug}}{\text{total amount of drug}} \times 100\%$$

$$\mathrm{DL}(\%) = \frac{\text{total amount of drug-amount of free drug}}{\text{total amount of nanoparticles}} \times 100\%$$

2.4 *In Vitro* degradation behavior of HM and drug release behavior of H@G

The degradation behavior of HM was evaluated using a UV-Vis spectrophotometer under different media (pH 7.4 PBS, pH 6.5 PBS, pH 7.4 and pH 6.5 PBS with 100 μM H_2O_2, and DMEM/F12 complete medium) and incubated at 37 °C. At predetermined time points (0.5, 1, 2, 4, 8, 12, and 24 h), the absorbance at approximately 400 nm was measured to determine the remaining fraction of HM.[25,28]

The release behavior of 6-gingerol from H@G was evaluated using a centrifugal method under different media (pH 7.4 PBS, pH 6.5 PBS, pH 7.4 and pH 6.5 PBS with 100 μM H_2O_2, and DMEM/F12 complete medium), each supplemented with Tween 80 to maintain sink conditions for the 6-gingerol. The suspensions were incubated at 37 °C with gentle shaking (100 rpm). At predetermined time points (0.5, 1, 2, 4, 8, 12, and 24 h), the samples were centrifuged at 12 000 rpm for 10 min. The supernatant was carefully collected, and the concentration of released 6-gingerol was determined by HPLC at 280 nm. At each time point, the pellet was resuspended in fresh release medium to continue the release study. The cumulative release percentage was calculated using a calibration curve prepared from standard solutions of 6-gingerol in the respective release medium. All experiments were performed in triplicate.

2.5 Material characterization

The morphology and structure of the nanoparticles were examined by scanning electron microscopy (SEM, ZEISS Sigma 360, Germany) and transmission electron microscopy (TEM, JEOL JEM-F200, Japan). Elemental composition was analyzed using energy-dispersive X-ray spectroscopy (EDS, Oxford X-Max 80T) coupled with the SEM. Measurements were conducted using a dynamic light scattering system (Malvern Nano-ZS90, UK) as follows: particle size distribution for HM and H@G(HM, H@G); zeta potential in deionized water; zeta potential in PBS (samples HM/PBS and H@G/PBS); and zeta potential in culture medium (samples HM/DF and H@G/DF). The surface elemental valence states were determined by X-ray photoelectron spectroscopy (XPS, Thermo Fisher ESCALAB Xi+, USA). Chemical bonds were characterized by Fourier transform infrared spectroscopy (FTIR, SHIMADZU IR Tracer-100, Japan). Specific surface area and pore size distribution were analyzed *via* the Brunauer–Emmett–Teller (BET) and Barrett–Joyner–Halenda (BJH) methods using a gas sorption analyzer (Microtrac BELSORP MAX II, Japan).

2.6 Enzyme activity assays

The superoxide dismutase (SOD)-like activity of H@G was assessed using a commercial kit based on the xanthine oxidase-NBT system. Principle: Xanthine is catalyzed by xanthine oxidase to generate superoxide anions ($O_2^{\bullet -}$), which reduce NBT to blue formazan with an absorption peak at 560 nm; SOD scavenges $O_2^{\bullet -}$ and thus inhibits formazan formation. Procedure: H@G samples were mixed with the reaction buffer, and the reaction was initiated by adding xanthine oxidase. After incubation at 37 °C for 30 min, the absorbance at 560 nm was measured. Lower absorbance indicates higher SOD-like activity.[29]

The hydroxyl radical ($^{\bullet}OH$) scavenging activity was evaluated using a Fenton reaction-based kit. Principle: H_2O_2 and Fe^{2+} generate $^{\bullet}OH$, which reacts with salicylic acid to form a colored product with maximum absorbance at 510 nm. Procedure: H@G samples were incubated with the reaction mixture at 37 °C for 1 h. After centrifugation, the absorbance at 510 nm was recorded. A decrease in absorbance reflects $^{\bullet}OH$ scavenging activity.[30]

The catalase (CAT)-like activity was determined using a hydrogen peroxide assay kit (titanium sulfate method). Principle: Residual H_2O_2 reacts with titanium sulfate to form a yellow peroxo–titanium complex with absorbance at 410 nm. Procedure: H@G samples were incubated with 800 μM H_2O_2 in PBS at 37 °C for 30 min, followed by addition of titanium sulfate solution. The absorbance at 410 nm was measured. Lower absorbance indicates higher CAT-like activity.[31]

2.7 Isolation and culture of rat nucleus pulposus cells

All animal procedures were performed in accordance with the Guidelines for the Care and Use of Laboratory Animals of North Sichuan Medical College and approved by the Animal Ethics Committee of North Sichuan Medical College. NPCs were isolated from the caudal vertebrae of male Sprague-Dawley rats (SD rats). The animals were euthanized by intraperitoneal injection of 3% sodium pentobarbital. Under aseptic conditions in a laminar flow hood, the tail was disinfected, and the nucleus pulposus (NP) tissue from each intervertebral disc was carefully extracted. The collected tissue was minced and digested in 0.2% type II collagenase solution at 37 °C for 2 hours. The resulting cell suspension was centrifuged at 800 rpm for 5 minutes to pellet the cells. The isolated NPCs were cultured in DMEM/F12 medium supplemented with 10% FBS and 1% penicillin/streptomycin, and maintained at 37 °C in a humidified incubator with 5% CO_2. The culture medium was changed every other day. Cells were passaged at 80–90% confluence, and NPCs from passages 2–3 were used for all subsequent *in vitro* experiments.

2.8 *In Vitro* cytotoxicity assessment

2.8.1 Biocompatibility of HM and H@G. NPCs were seeded into 96-well plates at a density of 5×10^3 cells per well and allowed to adhere for 24 hours. The cells were divided into several groups: a normal control (NC) group without any treatment, and experimental groups treated with various concentrations of HM or H@G. After treatment for 24 or 72 hours, cell viability was quantified using a Cell Counting Kit-8 (CCK-8) assay according to the manufacturer's instructions. Absorbance was measured at 450 nm using a microplate reader.

For qualitative assessment of cell viability, a live/dead staining assay (Calcein-AM/Propidium Iodide) was performed. NPCs were seeded in 24-well plates at 1×10^4 cells per well. After a 24-hour treatment with H@G, cells were washed with

PBS and incubated with the staining solution at room temperature for 30 minutes. Fluorescent images were captured using a fluorescence microscope.

2.8.2 Protective effect of H@G against H_2O_2-Induced injury. NPCs were seeded into 96-well plates at a density of 5×10^3 cells per well and cultured for 24 hours to allow for adhesion. After this attachment period, the cells were pre-treated with different concentrations of H@G for 1 hour, followed by exposure to 100 μM H_2O_2 for 24 hours to induce oxidative injury. Cell viability was then assessed at 24 and 72 hours post-H_2O_2 challenge using the CCK-8 assay. In parallel, a live/dead staining assay was performed according to the same treatment protocol as described in Section 2.8.1 to qualitatively evaluate cell survival and death.

2.9 Analysis of oxidative stress and mitochondrial function

2.9.1 Intracellular ROS detection. NPCs were seeded in 24-well plates at 1×10^4 cells per well. After a 1 hour pre-incubation with different concentrations of H@G, the cells were further incubated in medium containing 100 μM H_2O_2 for 24 hours. Cells were washed with PBS and incubated with a DCFH-DA fluorescent probe (ROS assay kit) at 37 °C for 15 minutes. ROS levels were visualized and imaged using a confocal microscope and quantified by flow cytometry.

2.9.2 Mitochondrial ROS detection. NPCs were seeded in confocal dishes at 2×10^4 cells per well. After pretreatment with varying concentrations of H@G for 1 hour, the cells were subsequently challenged with 100 μM H_2O_2 for 24 hours. Cells were washed with PBS and incubated with the MitoSOX Red mitochondrial superoxide indicator (5 μM) at 37 °C in the dark for 20 minutes. Following a PBS wash, mitochondrial superoxide levels were observed using confocal microscopy and quantified by flow cytometry.

2.9.3 Mitochondrial membrane potential ($\Delta\Psi_m$) assessment. Changes in $\Delta\Psi_m$ were monitored using the JC-1 fluorescent dye. Treated NPCs in 24-well plates were incubated with JC-1 staining solution at 37 °C for 30 minutes. After washing, the ratio of red (aggregates, high $\Delta\Psi_m$) to green (monomers, low $\Delta\Psi_m$) fluorescence was observed under a fluorescence microscope to indicate mitochondrial health.

2.9.4 Mitochondrial morphology by TEM. Treated NPCs were collected and fixed with 2.5% glutaraldehyde at 4 °C overnight. After washing with PBS, samples were post-fixed with 1% osmium tetroxide, dehydrated through a graded ethanol and acetone series, and embedded in epoxy resin 812. Ultrathin sections (60–80 nm) were prepared using an ultramicrotome, double-stained with uranyl acetate and lead citrate, and observed under a TEM to examine mitochondrial ultrastructure.

2.9.5 Intracellular ATP level measurement. After the indicated treatments, NPCs were washed with PBS, and intracellular ATP levels were measured using an ATP assay kit according to the manufacturer's instructions. Briefly, cells were lysed with the provided lysis buffer, and the lysates were centrifuged to collect the supernatants. After adding the chromogenic reagent, the absorbance was measured at 700 nm using a microplate reader to determine the ATP content.

2.10 Cellular immunofluorescence staining

The cells were washed with PBS and fixed with 4% neutral formaldehyde for 15 min at room temperature. After washing with cold PBS, cells were permeabilized with 0.1–0.3% Triton X-100 for 20–30 min. Following PBS washes, samples were blocked with 5% BSA at 37 °C for 30 min. Then, the following corresponding primary antibodies diluted in appropriate buffer were added: COL2A1 (1 : 200), ACAN (1 : 400), MMP3 (1 : 200), MMP13 (1 : 200). The samples were incubated overnight at 4 °C. The next day, after warming and washing with PBST and PBS, the samples were incubated with a species-matched fluorescent secondary antibody (Goat Anti-Rabbit IgG H&L) at 37 °C for 1 h in the dark. After further washes, nuclei were counterstained with DAPI. Finally, samples were mounted with an anti-fade mounting medium and imaged using a confocal microscope.

2.11 Statistical analysis

All quantitative data are presented as the mean ± standard deviation (SD) from at least three independent experiments. Statistical comparisons among multiple groups were performed using one-way analysis of variance (ANOVA) followed by Tukey's post hoc test in GraphPad Prism software. A *p*-value of less than 0.05 was considered statistically significant.

3 Results

3.1 Morphology and structure characterizations of HM and H@G

A schematic diagram illustrating the synthesis of HM is shown in Fig. 1A. Monodisperse silica (SiO_2) nanoparticles were first synthesized *via* the hydrolysis of TEOS to serve as a hard template. These SiO_2 nanoparticles were subsequently reacted with $KMnO_4$, leading to the formation of a uniform MnO_2 shell

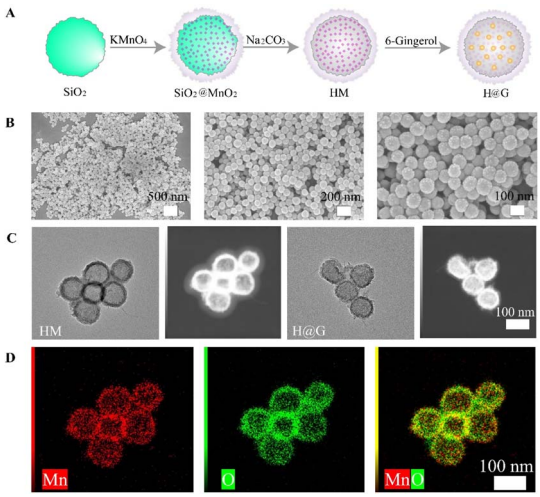

Fig. 1 Morphology and structure characterizations of HM and H@G. (A) Schematic diagram of HM synthesis. (B) SEM images of HM at different magnifications. (C) TEM micrograph and elemental mapping images of HM. (D) TEM micrograph and elemental mapping images of H@G.

on their surface and yielding core–shell structured MnO_2@SiO_2 nanoparticles. The silica core was then selectively etched by incubation with a Na_2CO_3 solution, resulting in the hollow manganese dioxide nanocarrier, designated HM. Finally, HM was thoroughly mixed with 6-gingerol to produce the drug-loaded composite, H@G. SEM images revealed that the synthesized HM nanoparticles were uniformly spherical and approximately 100 nm in diameter. This morphology demonstrated good consistency across different batches (Fig. 1B). TEM revealed that HM exhibited a uniform spherical morphology with a diameter of approximately 100 nm and a shell thickness of about 10 nm. Elemental mapping based on high-angle annular dark-field scanning transmission electron microscopy (HAADF-STEM) visually confirmed the hollow structure of HM. H@G maintained a hollow architecture similar to that of HM, with no appreciable change in morphology (Fig. 1C). The elemental mapping analysis indicated that HM was composed mainly of Mn and O, with both elements concentrated in the shell region (Fig. 1D). Thus, both HM and H@G possessed a well-defined hollow structure and homogeneous elemental distributions, demonstrating their potential as ideal nanocarriers.

3.2 Material characterizations of HM and H@G

DLS measurements indicated an increase in the hydrodynamic diameter of HM from 183 nm to 221 nm upon loading with gingerol (Fig. 2A and B). The zeta potential of the nanoparticles decreased from −37 mV for HM to −30 mV for H@G upon drug loading (Fig. 2C). Although the surface charge was reduced, the value of −30 mV still indicates good colloidal stability, which can be attributed to the physical adsorption of electrically neutral gingerol molecules onto the HM surface, partially shielding its negative charges. This maintained dispersity further confirms successful drug loading of H@G. XPS spectra of both HM and H@G confirmed the presence of O, Mn and C (Fig. 2D). High-resolution analysis of the Mn 2p region revealed binding energies at 643.39 eV, 642.12 eV, and 640.48 eV, corresponding to Mn^{4+}, Mn^{3+}, and Mn^{2+} valence states, respectively (Fig. 2E). Successful gingerol loading was further verified by FTIR spectroscopy (Fig. 2F). Compared to the spectrum of HM, the H@G spectrum displayed characteristic absorption peaks of gingerol, including the C–H stretching vibration at 2931 cm^{-1}, the aromatic C=C skeletal vibration at 1518 cm^{-1}, and the phenolic C–O stretching vibration at 1263 cm^{-1}. The BET surface area of HM was determined to be 74.3 $m^2\ g^{-1}$, with an average pore diameter of 7.39 nm (Fig. 2G). This high surface area and mesoporous structure provided abundant sites and sufficient space for efficient gingerol loading. The CCK-8 assay was conducted to assess the biocompatibility of HM. At a concentration of 50 μg mL^{-1}, cell viability showed a noticeable initial decrease on day 1 compared to the control group; however, it recovered and remained above 85% of the control level by day 3 (Fig. 2H and I). Based on these observations, a concentration of 50 μg mL^{-1} HM was selected for all subsequent experiments in this study.

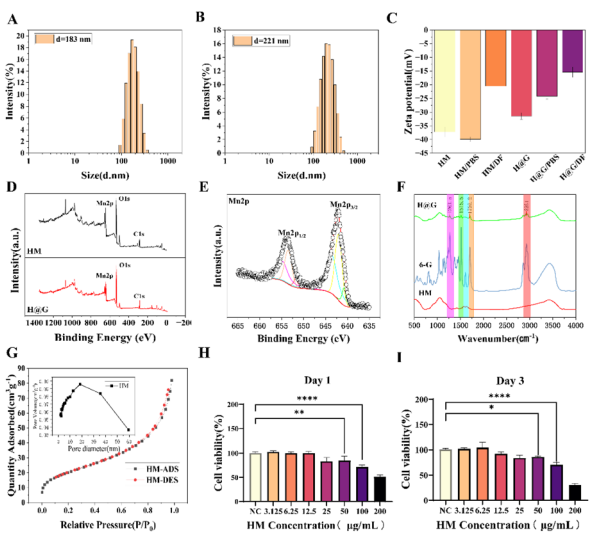

Fig. 2 Material characterization of HM and H@G. (A) Particle size distribution of HM. (B) Particle size distribution of H@G. (C) Zeta potential of HM and H@G in different solutions. (D) XPS total spectra of HM and H@G. (E) Valence state of manganese ions in HM. (F) FTIR spectra of HM, 6-G, and H@G. (G) Average pore size and nitrogen adsorption/desorption isotherms of HM. (H) (I) CCK-8 assay of HM on day 1 and day 3.

3.3 The degradation, drug loading and release of the nanoparticles

The degradation behavior of HM was evaluated using a UV-Vis spectrophotometer under different conditions. As shown in Fig. 3A, HM exhibited a rapid degradation phase within the first 2 h under all tested conditions, followed by a slower sustained degradation. At pH 7.4, HM remained relatively stable, with more than 90% of the nanoparticles retained after 24 h. Similarly, HM showed good stability in DMEM/F12 medium. In contrast, at pH 6.5, the nanoplatform degraded more rapidly, leaving only approximately 45% after 24 h. The presence of H_2O_2 further accelerated the degradation: at pH 7.4 with 100 μM H_2O_2, approximately 60% of HM remained after 24 h, whereas at pH 6.5 with 100 μM H_2O_2, only about 23% remained. Collectively, these results demonstrated that HM possessed good stability under physiological conditions but underwent accelerated and responsive degradation under pathological conditions such as acidic pH or the presence of H_2O_2 (Fig. 3A). Moreover, the drug loading and release performance of H@G were evaluated. H@G exhibited a drug loading content of 20.8% ± 1.8% and an encapsulation efficiency of 70.6% ± 6.2%, indicating that HM efficiently loaded 6-gingerol. As shown in Fig. 3B, the drug release behavior of H@G was evaluated under different conditions. H@G exhibited a low cumulative release of 6-gingerol under physiological conditions (pH 7.4 and DMEM/F12 complete medium), with less than 20% released within 24 h. In contrast, at pH 6.5, the release rate was significantly accelerated, achieving approximately 60% release within 24 h. Furthermore, the presence of 100 μM H_2O_2 further enhanced the release under acidic conditions, reaching nearly 75% within 24 h. These results demonstrated that H@G possessed pH- and

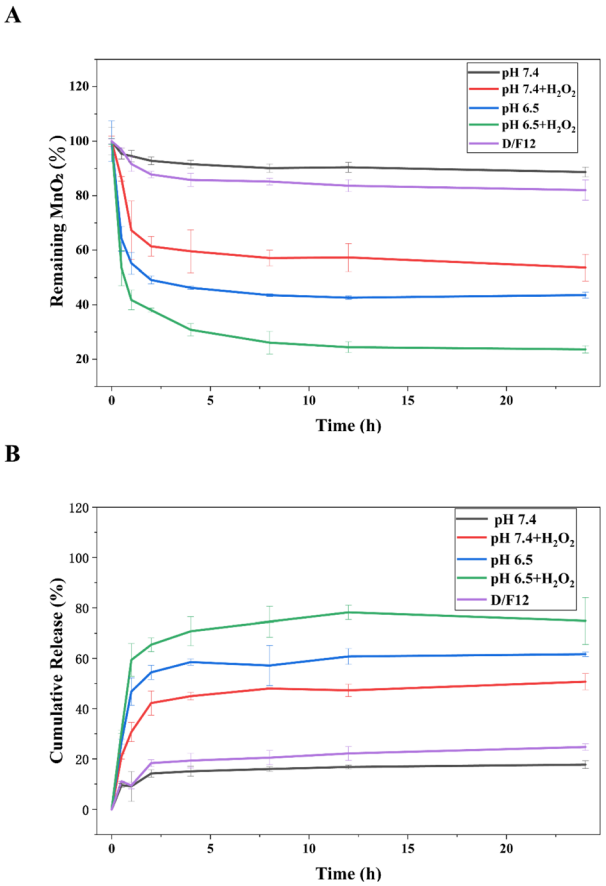

Fig. 3 (A) The degradation curves of HM under different conditions (pH 7.4 PBS, pH 7.4 PBS with 100 μM H_2O_2, pH 6.5 PBS, pH 6.5 PBS with 100 μM H_2O_2, and DMEM/F12 complete medium). (B) Drug release profiles of H@G under different conditions (pH 7.4 PBS, pH 7.4 PBS with 100 μM H_2O_2, pH 6.5 PBS, pH 6.5 PBS with 100 μM H_2O_2, and DMEM/F12 complete medium).

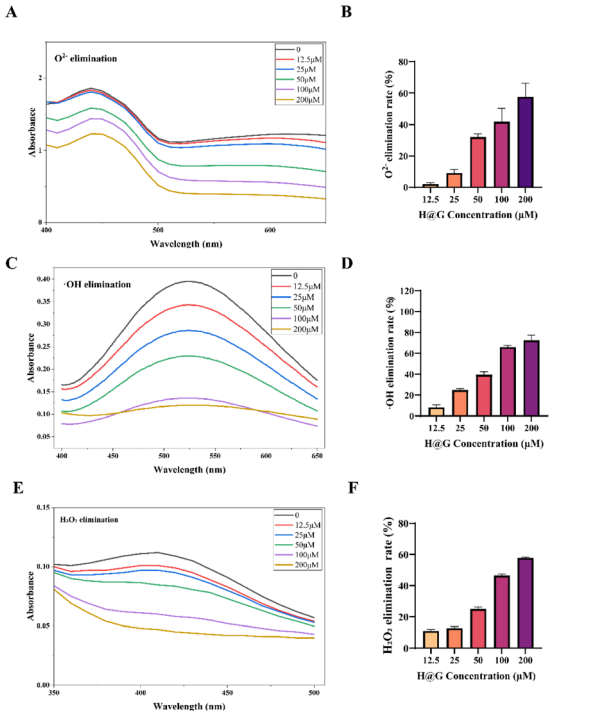

Fig. 4 Enzyme activity assays of H@G. (A) Absorbance spectra of SOD detection; (B) quantitative analysis of $O_2^{\bullet-}$ scavenging rate; (C) absorbance spectra of ·OH scavenging; (D) quantitative analysis of ·OH scavenging rate. (E) Absorbance spectra of catalase-like activity (H_2O_2 scavenging); (F) quantitative analysis of H_2O_2 scavenging rate.

H_2O_2-responsive release profile, enabling minimal drug leakage under normal physiological conditions while achieving rapid and targeted drug release in the acidic and oxidative microenvironment characteristic of degenerated intervertebral discs.

3.4 Enzyme activity of H@G

The enzyme-like activities of H@G were evaluated as shown in Fig. 4A. H@G exhibited a potent scavenging capacity against $O_2^{\bullet-}$, and the absorbance at 560 nm decreased with increasing concentration (Fig. 4A). At a concentration of 200 μM, H@G achieved an $O_2^{\bullet-}$ scavenging rate of approximately 60% (Fig. 4B). For ·OH scavenging, H@G displayed a similar trend; the absorbance at 510 nm decreased as the concentration of H@G increased, with the lowest absorbance observed at 200 μM, and the ·OH scavenging rate reached nearly 75% (Fig. 4C and D). As shown in Fig. 4E and F, H@G efficiently scavenged H_2O_2 in a concentration-dependent manner. The absorbance at 410 nm decreased progressively with increasing H@G concentration, and the H_2O_2 scavenging rate reached approximately 60% at 200 μM (Fig. 4F). These results demonstrated that H@G possessed catalase-like activity, complementing its SOD-like and hydroxyl radical-scavenging capacities and enabling broad-spectrum ROS elimination.

3.5 Cytocompatibility of H@G

The cytocompatibility of H@G was assessed by live/dead staining and CCK-8 assays. Fluorescence imaging revealed that after 24-hour exposure to both high and low-concentration H@G, the density of viable cells (stained green) remained comparable to that in the untreated control group, indicating no marked cytotoxic effect (Fig. 5A and C). Consistent with these observations, quantitative CCK-8 analysis showed a statistically significant yet transient decrease in NPC viability across all H@G-treated groups at 24 h (Fig. 5B).

Importantly, by day 3, cell viability in all H@G-treated groups (across various concentrations) had recovered to levels comparable to the control. Moreover, in the 10, 100, and 200 μM groups, viability was even moderately elevated relative to the control (Fig. 5D). Together, these results confirmed the favorable biocompatibility and minimal cytotoxicity of the H@G nanocarrier system over extended culture periods.

3.6 Protective effect of H@G against H_2O_2-Induced injury

To evaluate the protective effect of H@G on NPCs under oxidative stress, cell viability was assessed using CCK-8 and live/dead staining following H_2O_2 stimulation (Fig. 6). H_2O_2, a well-established inducer of oxidative stress, can lead to

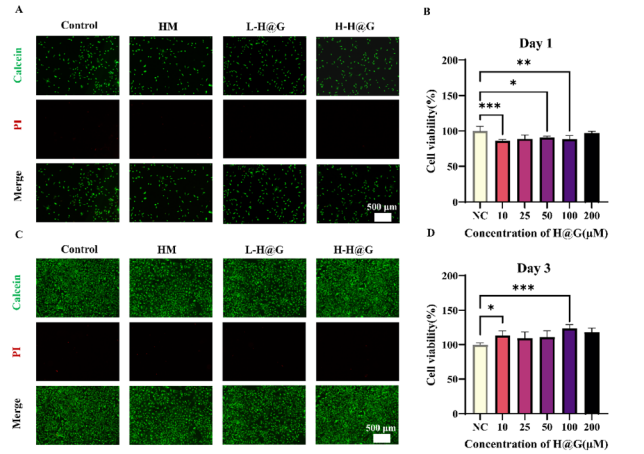

Fig. 5 Cytotoxicity assay across different groups. (A) and (B) Day 1 live/dead staining and CCK-8 results for nucleus pulposus cells across different groups. (C) and (D) Day 3 live/dead staining and CCK-8 results for nucleus pulposus cells across different groups.

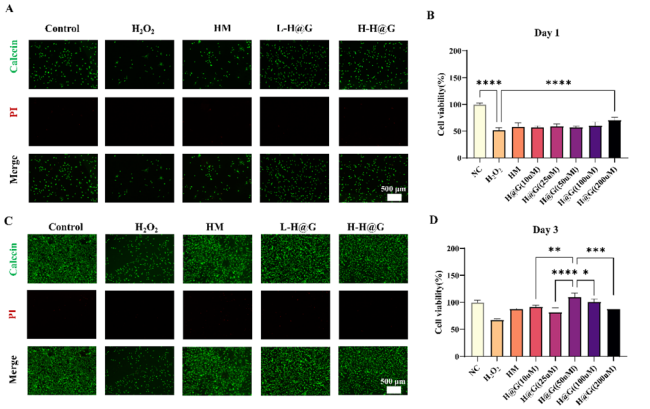

Fig. 6 Cell recovery experiment. (A) and (B) Day 1 live/dead staining and CCK-8 assay results for nucleus pulposus cells across different groups. (C) and (D) Day 3 live/dead staining and CCK-8 assay results for nucleus pulposus cells across different groups.

mitochondrial dysfunction and cellular senescence.[30] Based on prior studies, a concentration of 100 μM H_2O_2 was selected for establishing the injury model.[32] NPCs were pre-treated with the respective formulations for 1 day, followed by exposure to 100 μM H_2O_2; viability was then measured at 1 and 3 days post-H_2O_2 challenge. CCK-8 results indicated that at 1 day, cell viability declined across all groups exposed to H_2O_2. However, by 3 days, NPCs were pre-treated with the respective formulations for 1 day, followed by exposure to 100 μM H_2O_2; viability was then assessed at 1 and 3 days post-challenge. Live/dead staining revealed that while the H_2O_2-only group exhibited a substantial reduction in viable cells, the H–H@G group maintained a high proportion of live cells, with viability levels comparable to those of the untreated control group (Fig. 6A and C). Correspondingly, CCK-8 results indicated that at 1 day, cell viability declined across all groups exposed to H_2O_2. However, by 3 days, NPCs pre-treated with H@G showed a significant concentration-dependent recovery in viability. In contrast, cells treated with HM alone displayed only partial recovery compared to the H_2O_2 group, while the combined system (H@G) exhibited significantly higher cell viability at both time points (Fig. 6B and D).

This suggested that the protective effect of H@G surpasses that of the carrier alone, supporting a synergistic contribution from the loaded gingerol. Notably, the group treated with 50 μM H@G demonstrated the most significant restorative effect, with cell viability not only returning to but even surpassing that of the untreated control group, indicating a potential pro-proliferative benefit. Consequently, 50 μM H@G (corresponding to a mass concentration of 60.4 μg mL^{-1}) was selected as the primary experimental concentration (designated H–H@G), while 10 μM H@G served as a lower-concentration control (L–H@G) for subsequent experiments.

3.7 Assessment of the antioxidant capacity of H@G

To assess the protective role of H@G against oxidative stress, an *in vitro* oxidative damage model was established using H_2O_2. Intracellular ROS levels were detected using a fluorescent probe. As shown in Fig. 7A and B, cells in the control group exhibited weak baseline fluorescence. In contrast, H_2O_2 treatment induced a marked increase in fluorescence intensity, confirming successful accumulation of intracellular ROS and establishment of the oxidative stress model. Treatment with the different formulations resulted in varying degrees of reduction in ROS-associated fluorescence. Compared to the HM-treated group, which moderately reduced ROS levels, H@G caused a markedly greater decrease in intracellular ROS fluorescence intensity (Fig. 7A–C). The superior ROS-scavenging capacity of

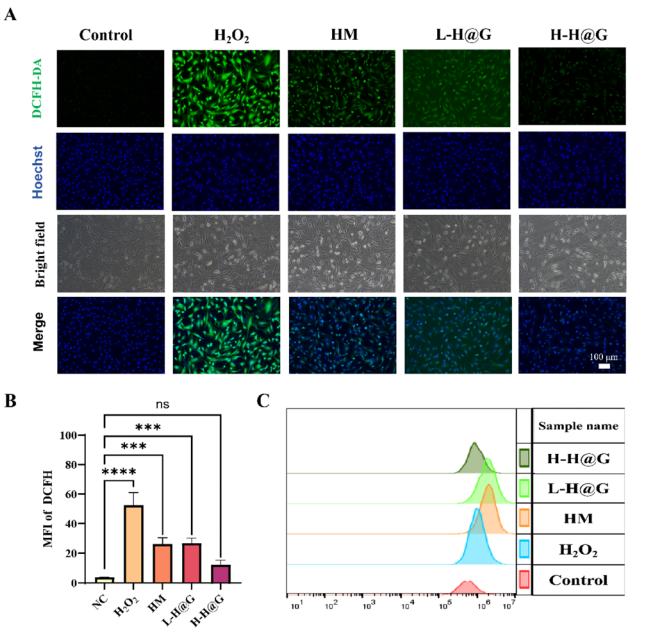

Fig. 7 Assessment of H@G's antioxidant stress capacity. (A) ROS fluorescence staining across different groups. (B) Semi-qua titative analysis of ROS fluorescence staining. (C) Flow cytometry analysis of ROS across different groups.

H@G over HM alone indicated that gingerol release enhances the antioxidative activity of the system. Quantitative analysis by flow cytometry (Fig. 7C) corroborated these observations, demonstrating that H@G, particularly at the higher concentration, effectively scavenged the excess ROS induced by H_2O_2.

3.7.1 H@G preserves mitochondrial ultrastructure and membrane potential. TEM analysis directly revealed the impact of H_2O_2 and subsequent treatments on mitochondrial morphology in NPCs. Mitochondria in the control group exhibited an elongated shape with well-defined cristae, orderly arrangement, and uniform matrix density. H_2O_2 stimulation induced severe structural damage, including a marked reduction in cristae number and disorganization of the matrix. While HM partially attenuated mitochondrial swelling and cristae loss, the structural preservation in the H–H@G group was far more pronounced and closely resembled that of the normal control group.

Fig. 8A mitochondrial functional integrity was further assessed by measuring the membrane potential using JC-1 staining. In control cells, the predominant red fluorescence (JC-1 aggregates) over minimal green fluorescence (JC-1 monomers) indicated a high mitochondrial membrane potential. H_2O_2 exposure caused a sharp decline in the red/green fluorescence ratio, reflecting severe mitochondrial depolarization. Similarly, JC-1 staining revealed that HM treatment alone did not significantly restore the depolarized membrane potential induced by H_2O_2, whereas H–H@G treatment nearly normalized the red/green fluorescence ratio, signaling a substantial functional rescue (Fig. 8B and C).

3.7.2 H@G alleviates mitochondrial oxidative stress. The level of mitochondrial oxidative stress was evaluated using MitoSOX Red, a fluorescent probe specific for mitochondrial superoxide. Control mitochondria displayed minimal MitoSOX fluorescence. H_2O_2 stimulation triggered a substantial

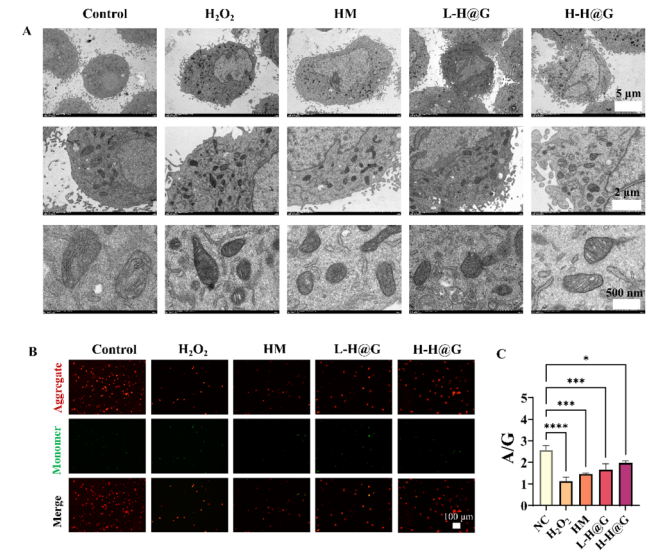

Fig. 8 Mitochondrial structure and membrane potential. (A) Transmission electron microscopy images of mitochondria. (B) JC-1 staining of mitochondrial membrane potential in nucleus pulposus cells. (C) Semi-quantitative fluorescence analysis of JC-1.

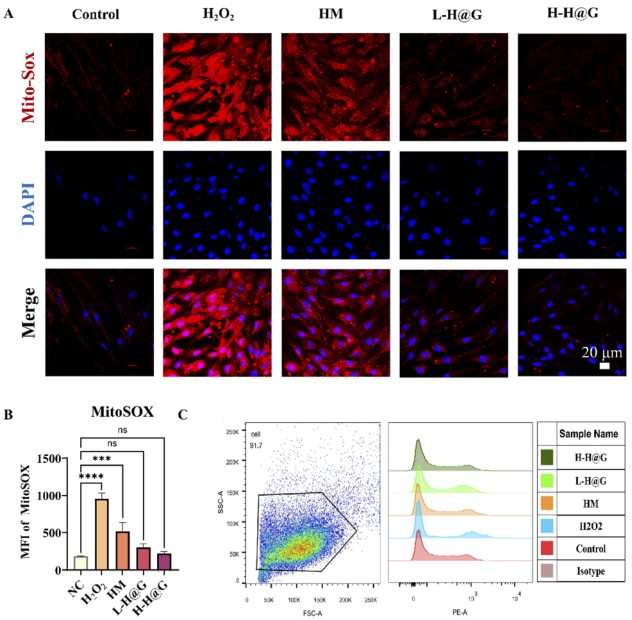

Fig. 9 Mitochondrial ROS. (A) Mitochondrial ROS-MitoSOX fluorescence staining. (B) Semi-quantitative fluorescence analysis of mitochondrial ROS-MitoSOX. (C) Mitochondrial MitoSOX flow cytometry.

increase in fluorescence, confirming a burst of ROS within the organelles. This oxidative stress was progressively mitigated by treatment with HM, L–H@G, and H–H@G, with the H–H@G group eliminating the majority of the excess ROS (Fig. 9A and B). Quantitative flow cytometry confirmed that H@G reduced mitochondrial superoxide levels more effectively than HM alone at equivalent carrier concentrations (Fig. 9C). This indicated that gingerol loading substantially enhances the ability of the nanoplatform to mitigate mitochondrial-specific oxidative stress. To further evaluate the impact of H@G on mitochondrial bioenergetics, intracellular ATP levels were measured. Compared with the NC group, H_2O_2 exposure significantly reduced ATP content; treatment with HM alone partially restored ATP levels, whereas both free 6-gingerol (6-G) and L-H@G further significantly increased ATP levels compared to HM, and H–H@G exhibited the most pronounced recovery, bringing ATP levels closest to those of the NC group (SI Fig. S3).

In summary, H_2O_2 exposure induced comprehensive mitochondrial damage, encompassing structural disintegration, loss of membrane potential, ROS overproduction, and ATP depletion. Intervention with H–H@G effectively counteracted these pathological changes, restoring cristae architecture, recovering membrane polarization, markedly scavenging excess ROS, and replenishing intracellular ATP levels, thereby demonstrating a potent protective effect on mitochondrial integrity and function under oxidative stress.

3.8 H@G restores extracellular matrix homeostasis in NPCs under oxidative stress

To further investigate the impact of H@G on extracellular matrix (ECM) metabolism in NPCs, we assessed the expression

levels of the anabolic markers ACAN and COL2A1, as well as the catabolic markers MMP3 and MMP13, *via* immunofluorescence staining. In the control group, both ACAN and COL2A1 exhibited strong fluorescent signals, indicating robust matrix synthesis. Co-culture with H_2O_2 significantly attenuated the fluorescence intensity of both proteins, suggesting that oxidative stress severely suppressed the anabolic function of NPCs. The expression of these anabolic markers in the HM group showed no significant difference from the H_2O_2 group. However, a partial recovery was observed in the L–H@G group, and the recovery was most pronounced in the H–H@G group, where the fluorescence intensity was restored to a level closest to that of the control (Fig. 10A).

In contrast, the expression of the catabolic markers displayed an opposite trend. Fluorescence signals for MMP3 and MMP13 were barely detectable in the control group. However, H_2O_2 stimulation strongly induced their expression, resulting in a sharp increase in fluorescence intensity. The expression of both catabolic markers remained elevated in the HM group compared to the Control. Intervention with either L–H@G or H–H@G effectively reversed this abnormal upregulation. Again, the H–H@G group showed the most notable effect, with MMP3 and MMP13 expression reduced to levels comparable to the Control (Fig. 10B).

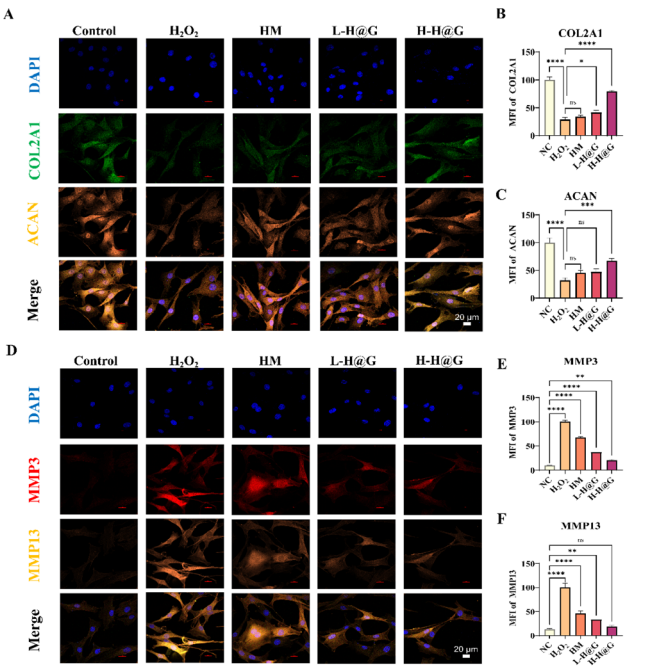

Fig. 10 Immunofluorescence staining of extracellular matrix markers. (A) Immunofluorescence staining of extracellular matrix markers COL2A1 and ACAN. (B) Semi quantitative analysis of COL2A1 immunofluorescence. (C) Semi quantitative analysis of ACAN immunofluorescence. (D) Immunofluorescence staining of extracellular matrix degradation markers MMP3 and MMP13. (E) Semi quantitative analysis of MMP3 immunofluorescence. (F) Semi quantitative analysis of MMP13 immunofluorescence.

4 Discussion

Intervertebral disc degeneration (IVDD), characterized by progressive extracellular matrix degradation and loss of NPC function, underlies chronic low back pain and associated neurological deficits.[3] The pathogenesis of IVDD is multifactorial, involving genetic predisposition, mechanical overloading, aging, compromised nutrient supply, and disruption of tissue homeostasis.[33] Among these, oxidative stress has been established as a central driver throughout the degenerative cascade.[34] The intervertebral disc exists in a unique avascular, hypoxic, and hyperosmotic microenvironment. Within this setting, NPCs maintain active metabolism but possess a relatively limited endogenous antioxidant capacity, rendering them particularly vulnerable to the generation and accumulation of excessive ROS under pathological stimuli.[35] These ROS inflict direct damage on cellular macromolecules including proteins, lipids, and DNA. More critically, they induce mitochondrial dysfunction, disrupt cellular energy metabolism, and activate key inflammatory and senescence-related signaling pathways, such as NF-κB and p53/p21.[13,36] This culminates in an imbalance between ECM synthesis and degradation, characterized by suppressed anabolic gene expression (*e.g.*, COL2A1 and ACAN) and elevated catabolic enzyme activity, promotes NPC senescence or death, and establishes a self-perpetuating vicious cycle of degeneration. Consequently, there is a pressing need for the development of highly efficient and targeted therapeutic strategies capable of synergistically modulating multiple pathological pathways at the critical nexus of oxidative stress to potentially halt or slow IVDD progression.

To address this unmet need, we designed and characterized an integrated nanoplatform (H@G) by encapsulating 6-G within HM, which demonstrated excellent biocompatibility and foundational safety for potential application. This system was designed with a two-fold strategy: first, to utilize HM as a responsive nanocarrier platform for the efficient loading and *in situ* release of gingerol; and second, to harness the combined intrinsic catalytic activity of HM and the multifaceted bioactivity of gingerol to synergistically mitigate oxidative stress and its downstream sequelae in NPCs. Material characterization confirmed the successful synthesis of HM nanoparticles with uniform size, high specific surface area, and a well-defined hollow structure. The large cavity and mesoporous shell provided an ideal scaffold for loading the hydrophobic gingerol. Successful drug loading was further verified by FTIR spectroscopy, which displayed characteristic gingerol absorption peaks, alongside consistent shifts in hydrodynamic diameter and zeta potential. H@G also possessed enzyme–mimetic activities. As shown in Fig. 4, H@G exhibited concentration-dependent scavenging capacities against $O_2^{\bullet-}$, $^{\bullet}OH$, and H_2O_2, with scavenging rates reaching approximately 60%, 75%, and 60% at 200 μM, respectively. These SOD-like, $^{\bullet}OH$-scavenging, and CAT activities endow H@G with a broad-spectrum antioxidant capability, enabling it to target multiple ROS species simultaneously. Most importantly, CCK-8 and live/dead assays demonstrated that H@G exhibited no significant cytotoxicity

against NPCs at effective concentrations (*e.g.*, 50 μM), confirming its excellent biocompatibility and establishing a critical safety foundation for subsequent functional application. Since no obvious cytotoxicity was observed for H@G at concentrations up to 200 μM over 3 days, and the cell protection assay revealed that 50 μM H@G exhibited the strongest protective effect against H_2O_2-induced injury, we selected 50 μM as the high working concentration (designated H–H@G) and 10 μM as the low concentration control (L–H@G) for subsequent experiments to achieve optimal protective efficacy.

The degradation and drug release behavior of nanoparticles in various microenvironments play an important role in their therapeutic effects. The degradation results revealed that HM remained stable in physiological media but underwent accelerated degradation under acidic conditions (pH 6.5), with only approximately 45% remaining after 24 h. The degradation was further accelerated in the presence of H_2O_2. This pH- and H_2O_2-sensitive behavior is particularly relevant for the inflamed or degenerated intervertebral disc microenvironment, where local acidosis often accompanies oxidative stress and inflammation.[37,38] Leveraging this property, H@G exhibited negligible release under neutral conditions (pH 7.4 and DMEM/F12 complete medium), whereas the release was markedly accelerated under acidic conditions (pH 6.5), and the presence of H_2O_2 further promoted the release rate. Such a responsive profile minimizes premature drug leakage during systemic circulation or injection and enables on-demand gingerol release specifically within the pathological disc niche. Moreover, the high specific surface area (74.3 $m^2\ g^{-1}$) and mesoporous structure (average pore diameter 7.39 nm) of HM allowed a high drug loading content of 20.8% and encapsulation efficiency of 70.6%, which are favorable for reducing the required dose of nanocarrier and potential off-target effects. Collectively, these material properties establish HM as an intelligent, microenvironment-responsive delivery platform that synergizes with its catalytic activity.

In vitro assessments revealed that H@G conferred multitarget protection against oxidative injury, primarily through a potent and synergistic antioxidant mechanism and by preserving vital mitochondrial structure and function. At the primary defense level of direct ROS scavenging, fluorescence staining (DCFH-DA and MitoSOX) coupled with flow cytometry confirmed that H_2O_2 stimulation triggered a sharp increase in both intracellular and mitochondrial ROS, which was significantly attenuated by H@G treatment in a dose-dependent manner. This potent antioxidant capacity likely arose from a synergistic mechanism between the nanocarrier and its payload. Hollow-structured MnO_2 nanomaterials are known to exhibit catalase (CAT)-like activity, efficiently catalyzing the decomposition of H_2O_2 into water and oxygen.[39] On the other hand, our enzyme activity assays further demonstrated that H@G possessed additional enzyme–mimetic activities, including SOD-like, $^{\bullet}OH$ scavenging, and CAT-like capacities, with scavenging rates reaching approximately 60%, 75%, and 60% for $O_2^{\bullet-}$, $^{\bullet}OH$, and H_2O_2 at 200 μM, respectively. Thus, a broad-spectrum ROS-scavenging mechanism is established, encompassing both "nanomaterial-catalyzed decomposition" and "molecular radical neutralization" by the loaded gingerol. This approach aligns with recent advancements in multifunctional nanozymes, such as the greigite-based system reported by Shi *et al.*, which employs synergistic SOD/CAT activities and polysulfide release to combat ROS and rescue senescent NPCs.[33] Furthermore, H@G effectively preserved mitochondrial integrity, which is crucial for cellular viability. Mitochondria are both the primary site of ROS generation and a major target of oxidative damage. Our JC-1 staining results confirmed that H_2O_2 induced significant depolarization of the mitochondrial membrane potential ($\Delta\Psi_m$) in NPCs, a hallmark of severe dysfunction that compromised ATP synthesis and could initiate apoptotic pathways.[34] Treatment with H@G, particularly at the higher dose, effectively reversed this collapse of $\Delta\Psi$m. Furthermore, MitoSOX Red staining, which specifically targets mitochondrial superoxide, demonstrated that H@G significantly alleviated oxidative stress within the organelles. TEM provided direct and compelling ultrastructural evidence. Mitochondria in control NPCs displayed an elongated morphology with well-defined, densely packed cristae. H_2O_2 stimulation caused pronounced swelling, distortion, and fragmentation or even loss of cristae. In contrast, intervention with H–H@G facilitated substantial recovery of mitochondrial architecture, with clearly discernible cristae re-established. Mitochondrial structural integrity underpins its essential functions in energy metabolism, calcium homeostasis, and regulation of cell death.[35] Therefore, by protecting mitochondria from oxidative damage, H@G helps to break the vicious cycle wherein ROS-induced mitochondrial injury leads to further ROS overproduction, thereby fundamentally safeguarding cellular energy supply and survival homeostasis.

Beyond preserving cellular and mitochondrial integrity, our findings demonstrated that H@G effectively rescued the dysregulated ECM metabolism in oxidatively stressed NPCs-a hallmark of IVDD pathology. The observed upregulation of anabolic markers (ACAN, COL2A1) and concurrent downregulation of catabolic enzymes (MMP3, MMP13) upon H@G treatment indicates a shift in cellular phenotype towards matrix restoration. This effect is likely secondary to the mitigation of oxidative stress and the improvement of mitochondrial bioenergetics, as a healthy metabolic state is a prerequisite for the energy-intensive process of ECM synthesis. By simultaneously targeting oxidative damage at its source (mitochondria) and correcting its downstream consequence (ECM breakdown), H@G addresses multiple facets of the degenerative cascade, positioning it as a comprehensive therapeutic candidate.

While this study demonstrates the potential of H@G in mitigating oxidative stress and its downstream effects in NPCs, several limitations should be acknowledged, which also point to directions for future research. First, although H@G showed efficacy in alleviating oxidative damage, preserving mitochondrial function, and restoring ECM homeostasis, the investigation did not delve deeply into the underlying molecular signaling networks. It remains to be determined whether the protective effects involve the modulation of specific pathways beyond the general reduction of ROS, such as the Nrf2-mediated antioxidant response, NF-κB-driven inflammation, or other

related processes like cellular autophagy.[40,41] Second, our current conclusions are mainly derived from functional assessments (*e.g.*, cell viability, mitochondrial morphology, and immunofluorescence staining of a few ECM markers). To gain a more comprehensive understanding of the protective mechanism of H@G, further validation of signaling pathways such as NF-κB and MAPK by western blot analysis is warranted in future studies. Finally, all validations were performed in a simplified two-dimensional *in vitro* culture system, which cannot fully replicate the complex three-dimensional, mechanically loaded, and nutrient-poor microenvironment of the human intervertebral disc *in vivo*. The therapeutic potential and safety of H@G ultimately require evaluation in a physiologically relevant animal model of disc degeneration.[42]

5 Conclusion

In summary, this study successfully developed an integrated nanotherapeutic system by loading 6-gingerol into HM nanocarriers. HM exhibited good stability under physiological conditions but rapid degradation in acidic and H_2O_2-rich environments, enabling pH- and H_2O_2-responsive drug release from H@G. H@G possessed concentration-dependent SOD-like, ˙OH-scavenging and catalase-like activities, indicating its good antioxidant capacity. *In vitro* cell culture demonstrated that H@G effectively protected nucleus pulposus cells from H_2O_2-induced oxidative injury by enhancing cell viability, scavenging intracellular and mitochondrial ROS, restoring mitochondrial membrane potential and ultrastructure, and rebalancing extracellular matrix metabolism. This work provides a proof of concept for a multifunctional nanoplatform that simultaneously targets oxidative stress, mitochondrial dysfunction, and ECM imbalance, offering a novel strategic approach for the potential treatment of IVDD.

Author contributions

Xu Liu, Bolin Lu, Yunqi Zhou: conceptualization, methodology, investigation, writing – original draft. Chengdong Zhang, Feng Shi: methodology, investigation, validation, supervision. Gang Feng: conceptualization, supervision. Xuwei Luo: conceptualization, investigation, writing – review & editing, funding acquisition. Dongqin Xiao: conceptualization, methodology, investigation, writing – review & editing, funding acquisition.

Conflicts of interest

The authors declare that they have no known competing financial interests or personal relationships that could have appeared to influence the work reported in this paper.

Data availability

The datasets used and/or analysed in this study are available from the corresponding author upon reasonable request.

Supplementary information (SI): the results of CCK-8 assay, ROS fluorescence staining, and intracellular ATP levels in nucleus pulposus cells after different treatments. See DOI: https://doi.org/10.1039/d6ra00597g.

Acknowledgements

This study was funded by National Natural Science Foundation of China (82002289), Health Commission of Sichuan Province Medical Science and Technology Program (25QNMP101), Sichuan Medical Association Medical Research Program (S20250088), Sichuan Provincial Medical Association Young Innovators Project (Q2024026), Applied Basic Research Program of Nanchong City (25YYJCYJ0054, 25YYJCYJ0060) and Fundamental Research Funds of China West Normal University (24kc006).

References

1 E. Kague, F. Turci, E. Newman, Y. Yang, K. R. Brown, M. S. Aglan, G. A. Otaify, S. A. Temtamy, V. L. Ruiz-Perez, S. Cross, C. P. Royall, P. E. Witten and C. L. Hammond, *Bone Res.*, 2021, **9**, 39.
2 K. Ma, S. Chen, Z. Li, X. Deng, D. Huang, L. Xiong and Z. Shao, *Osteoarthr. Cartil.*, 2019, **27**, 41–48.
3 M. V. Risbud and I. M. Shapiro, *Nat. Rev. Rheumatol.*, 2014, **10**, 44–56.
4 S. M. Rider, S. Mizuno and J. D. Kang, *Spine Surg. Relat. Res.*, 2018, **3**, 1–11.
5 J. P. Urban and S. Roberts, *Arthritis Res. Ther.*, 2003, **5**, 120–130.
6 S. Roberts, H. Evans, J. Trivedi and J. Menage, *J. Bone Joint Surg. Am.*, 2006, **88**(Suppl 2), 10–14.
7 M. A. Adams and P. J. Roughley, *Spine*, 2006, **31**, 2151–2161.
8 Y. Wang, M. Che, J. Xin, Z. Zheng, J. Li and S. Zhang, *Biomed. Pharmacother.*, 2020, **131**, 110660.
9 Y. Li, Lu Chen, Y. Gao, X. Zou and F. Wei, *Oxid. Med. Cell. Longev.*, 2022, **2022**, 1984742.
10 M. Giorgio, M. Trinei, E. Migliaccio and P. G. Pelicci, *Nat. Rev. Mol. Cell Biol.*, 2007, **8**, 722–728.
11 S. Reuter, S. C. Gupta and M. M. Chaturvedi, *Free Radic. Biol. Med.*, 2010, **49**, 1603–1616.
12 J. Kim, M. Xu, R. Xo, A. Mates, G. L. Wilson, A. W. Pearsall and V. Grishko, *Osteoarthr. Cartil.*, 2010, **18**, 424–432.
13 H. Zhou, C. Wu, Y. Jin, O. Wu, L. Chen, Z. Guo, X. Wang, Q. Chen, K. Y. H. Kwan, Y. M. Li, D. Xia, T. Chen and A. Wu, *J. Orthop. Transl.*, 2024, **49**, 181–206.
14 Y. Wang, H. Cheng, T. Wang, K. Zhang, Y. Zhang and X. Kang, *Cell Prolif.*, 2023, **56**, e13448.
15 D. Sakai and S. Grad, *Adv. Drug Deliv. Rev.*, 2015, **84**, 159–171.
16 S. B. G. Blanquer, D. W. Grijpma and A. A. Poot, *Adv. Drug Deliv. Rev.*, 2015, **84**, 172–187.
17 W. Liu, Z. Ma, Y. Wang and J. Yang, *Bioact. Mater.*, 2022, **23**, 274–299.
18 Z. Wang, C. Wu, J. Liu, S. Hu, J. Yu, Q. Yin, H. Tian, Z. Ding, G. Qi, L. Wang and H. Liguo, *Drug Deliv.*, 2022, **30**, 28–39.
19 Q. Chen, L. Feng, J. Liu, W. Zhu, Z. Dong, Y. Wu and Z. Liu, *Adv. Mater.*, 2018, **30**, 1707414.

20 M. Cheng, Y. Yu, W. Huang, M. Fang, Y. Chen, C. Wang, W. Cai, S. Zhang, W. Wang and W. Yan, *ACS Biomater. Sci. Eng.*, 2020, **6**, 4985–4992.
21 Z. Cheng, X. Xiong, Y. Zhou, F. Wu, Q. Shao, R. Dong, Q. Liu, L. Li and G. Chen, *Biomed. Pharmacother.*, 2022, **146**, 112491.
22 R. M. T. de Lima, A. C. D. Reis, A.-A. P. M. de Menezes, J. V. de O. Santos, J. W. G. de O. Filho, J. R. de O. Ferreira, M. V. O. B. de Alencar, A. M. O. F. da Mata, I. N. Khan, A. Islam, S. J. Uddin, E. S. Ali, M. T. Islam, S. Tripathi, S. K. Mishra, M. S. Mubarak and A. A. de C. Melo-Cavalcante, *Phytother Res.*, 2018, **32**, 1885–1907.
23 A. Zahoor, C. Yang, Y. Yang, Y. Guo, T. Zhang, K. Jiang, S. Guo and G. Deng, *Phytomedicine*, 2020, **76**, 153248.
24 M. Zhang, E. Viennois, M. Prasad, Y. Zhang, L. Wang, Z. Zhang, M. K. Han, B. Xiao, C. Xu, S. Srinivasan and D. Merlin, *Biomaterials*, 2016, **101**, 321–340.
25 G. Yang, L. Xu, Y. Chao, J. Xu, X. Sun, Y. Wu, R. Peng and Z. Liu, *Nat. Commun.*, 2017, **8**, 902.
26 Y. Li, Z. Zou, J. An, Q. Wu, L. Tong, X. Mei, H. Tian and C. Wu, *Drug Delivery*, 2022, **29**, 2498–2512.
27 J. Liu, C. Guo, C. Li, Q. Jia, Z. Xie, Z. Wang, H. Tian, Z. Li and L. Hao, *Front. Chem.*, 2023, **11**, 1249472.
28 S. A. Moon, B. K. Salunke, B. Alkotaini, E. Sathiyamoorthi and B. S. Kim, *IET Nanobiotechnol.*, 2015, **9**, 220–225.
29 Y. Sun, L. W. Oberley and Y. Li, *Clin. Chem.*, 1988, **34**, 497–500.
30 Y. Shi, H. Li, D. Chu, W. Lin, X. Wang, Y. Wu, K. Li, H. Wang, D. Li, Z. Xu, L. Gao, B. Li and H. Chen, *Adv. Sci.*, 2023, **10**, 2300988.
31 S. Nag, K. Saha and M. A. Choudhuri, *Plant Sci.: Int. J. Exp. Plant Biol.*, 2000, **157**, 157–163.
32 S. K. Tschoeke, M. Hellmuth, A. Hostmann, Y. Robinson, W. Ertel, A. Oberholzer and C.-E. Heyde, *J. Orthop. Res.*, 2008, **26**, 999–1006.
33 L. Frapin, J. Clouet, V. Delplace, M. Fusellier, J. Guicheux and C. L. Visage, *Adv. Drug Deliv. Rev.*, 2019, **149–150**, 49–71.
34 P. R. Angelova, *Free Radic. Biol. Med.*, 2021, **173**, 52–63.
35 Q. Xia, Y. Zhao, H. Dong, Q. Mao, L. Zhu, J. Xia, Z. Weng, W. Liao, Z. Hu, J. Yi, S. Feng, Y. Jiang and Z. Xin, *Biomed. Pharmacother.*, 2024, **174**, 116593.
36 Q. Xiang, Y. Zhao, J. Lin, S. Jiang and W. Li, *Exp. Mol. Med.*, 2022, **54**, 1067–1075.
37 H. T. J. Gilbert, N. Hodson, P. Baird, S. M. Richardson and J. A. Hoyland, *Sci. Rep.*, 2016, **6**, 37360.
38 Z. Ząbek, A. Wyczałkowska-Tomasik, K. Poboży, J. P. Adamus, G. Turek, M. Ząbek and L. Pączek, *Int. J. Mol. Sci.*, 2025, **26**, 9938.
39 S. Kumar, I. M. Adjei, S. B. Brown, O. Liseth and B. Sharma, *Biomaterials*, 2019, **224**, 119467.
40 Q. Ren, L. Chen, Y. Ma, Y. Huang and S. Wang, *Front. Immunol.*, 2025, **16**, 1563635.
41 A. T. Dinkova-Kostova and I. M. Copple, *Trends Pharmacol. Sci.*, 2023, **44**, 137–149.
42 Y. Xu, F. Cai, Y. Zhou, J. Tang, J. Mao, W. Wang, Z. Li, L. Zhou, Y. Feng, K. Xi, Y. Gu and L. Chen, *Sci. Adv.*, 2024, **10**, eado7249.